BAMS
Article

PERSIANN Dynamic Infrared–Rain Rate Model (PDIR) for High-Resolution, Real-Time Satellite Precipitation Estimation

Phu Nguyen, Eric J. Shearer, Mohammed Ombadi, Vesta Afzali Gorooh, Kuolin Hsu, Soroosh Sorooshian, William S. Logan, and Marty Ralph

ABSTRACT: Precipitation measurements with high spatiotemporal resolution are a vital input for hydrometeorological and water resources studies; decision-making in disaster management; and weather, climate, and hydrological forecasting. Moreover, real-time precipitation estimation with high precision is pivotal for the monitoring and managing of catastrophic hydroclimate disasters such as flash floods, which frequently transpire after extreme rainfall. While algorithms that exclusively use satellite infrared data as input are attractive owing to their rich spatiotemporal resolution and near-instantaneous availability, their sole reliance on cloud-top brightness temperature (T_b) readings causes underestimates in wet regions and overestimates in dry regions—this is especially evident over the western contiguous United States (CONUS). We introduce an algorithm, the Precipitation Estimations from Remotely Sensed Information Using Artificial Neural Networks (PERSIANN) Dynamic Infrared–Rain rate model (PDIR), which utilizes climatological data to construct a dynamic (i.e., laterally shifting) T_b–rain rate relationship that has several notable advantages over other quantitative precipitation-estimation algorithms and noteworthy skill over the western CONUS. Validation of PDIR over the western CONUS shows a promising degree of skill, notably at the annual scale, where it performs well in comparison to other satellite-based products. Analysis of two extreme landfalling atmospheric rivers show that solely IR-based PDIR performs reasonably well compared to other IR- and PMW-based satellite rainfall products, marking its potential to be effective in real-time monitoring of extreme storms. This research suggests that IR-based algorithms that contain the spatiotemporal richness and near-instantaneous availability needed for rapid natural hazards response may soon contain the skill needed for hydrologic and water resource applications.

https://doi.org/10.1175/BAMS-D-19-0118.1

Corresponding author: Phu Nguyen, ndphu@uci.edu

In final form 28 October 2019

AFFILIATIONS: Nguyen, Shearer, Ombadi, Gorooh, Hsu, Sorooshian—Center for Hydrometeorology and Remote Sensing, Department of Civil and Environmental Engineering, Henry Samueli School of Engineering, University of California, Irvine, Irvine, California; **Sorooshian**—Department of Earth Systems Science, University of California, Irvine, Irvine, California; **Logan**—International Center for Integrated Water Resources Management, Institute for Water Resources, U.S. Army Corps of Engineers, Alexandria, Virginia; **Ralph**—Center for Western Weather and Water Extremes, Scripps Institution of Oceanography, University of California, San Diego, La Jolla, California

Precipitation measurements with high spatiotemporal resolution are an important input for hydrometeorological and water resources studies, along with being a key component of decision-making in disaster management. Reliable and accurate high-resolution, near-real-time precipitation data are pivotal in monitoring and managing catastrophic disasters such as drought or flash floods, which frequently cause major socioeconomic impacts (Hong et al. 2007; Nguyen et al. 2014; Sun et al. 2018). Rain gauges and radars are the most popular sources for precipitation measurement/estimation although their distribution is limited over oceans, remote locations, and high-altitude regions. Rain gauges are globally sparse, especially in developing countries, while radar suffers from blockage by mountain obstructions, anomalous propagation, beam overshoot, and more. In recent decades, satellite-based precipitation products have proven to be an alternative of great potential to ground-based precipitation measurements by providing the first quasi-global estimations, except for the polar regions. Last, the availability of near-real-time, satellite-based precipitation data plays an essential role in many weather, climate (Funk et al. 2015), and hydrological modeling–based projects and studies (Behrangi et al. 2011).

Satellite-based precipitation algorithms utilize a variety of input data from several sensors onboard geosynchronous-Earth-orbiting satellites (GEOs) and low-Earth-orbiting satellites (LEOs). The primary sensors used in precipitation estimation measure longwave infrared (IR), visible (VIS), and passive microwave (PMW). Satellite observations do not provide direct readings of rain rate (RR)—an indirect relationship is used to link the probability and intensity of rainfall to the information gathered by one or multiple sensors. PMW observations are strongly tied to the object's physical properties, such as precipitable-sized particles. Thus, it provides more direct estimates of precipitation. Although PMW sensors are recognized as a reliable source for instantaneous precipitation estimations, their spatial and temporal resolutions are far coarser than IR/VIS readings. In essence, the spatiotemporal richness of IR and/or VIS satellite observations helps balance the relatively poor spatiotemporal resolution of PMW sensors and so they are an integral part of many precipitation estimation algorithms. However, despite their fine resolutions, VIS observations are insufficient to capture precipitation variability during the night while IR only provides information regarding brightness temperature T_b.

Over the last two decades, a number of widely used satellite-derived quantitative precipitation estimating products have been developed by combining the information gathered by various sensors on single or multiple platforms. For instance, some products primarily utilize PMW measurements as their input. These are the Climate Prediction Center (CPC) Morphing method (CMORPH; Joyce et al. 2004), the Global Satellite Mapping of Precipitation (GSMaP; Ushio et al. 2009), and the Tropical Rainfall Measuring Mission (TRMM) Multisatellite Precipitation Analysis (TMPA; Huffman et al. 2007). On the other hand, there also exists a number of IR-based products, such as the Precipitation Estimation from Remotely Sensed Information Using Artificial Neural Networks—Cloud Classification System (PERSIANN-CCS; Hong et al. 2004), the Hydro-Estimator (HE; Scofield and Kuligowski 2003), the Global Precipitation Index (GPI; Arkin and Meisner 1987), and the Self-Calibrating Multivariate Precipitation Retrieval (SCaMPR; Kuligowski 2002). Last, there are products that exist through the combination of previously existing precipitation-estimating algorithms, such as the Global Precipitation Measurement (GPM) mission's Integrated Multisatellite Retrievals for GPM (IMERG; Huffman et al. 2014).

While many of the IR-based methods developed to date show fair skill and promise, there exists potential for much improvement. For example, one of the most prominent challenges for IR retrievals is warm cloud detection, which often cannot be accurately identified due to their high T_b (Hong et al. 2004). In other words, warm clouds such as stratiform clouds can cause rain while having temperatures similar to those at Earth's surface, which makes the task of segmenting clouds from Earth's surface based on IR readings challenging. Hence, many methods either regularly fail to capture warm precipitation events or elect to set T_b threshold limits lower than warm precipitation temperatures, effectively reducing their detection rate to zero. Moreover, the occultation of seeder clouds by feeder clouds commonplace in instances of warm orographic precipitation is a major difficulty in quantitative precipitation estimation (QPE). In addition, as many IR-based algorithms do not have a built-in cloud-type model, nonprecipitating cold clouds such as cirrus clouds with low T_b values will falsely be detected as a source of precipitation, which results in overestimating the occurrence and amount of precipitation (Hong et al. 2007).

Arguably, the primary limitation with IR-based algorithms is their reliance on T_b without the incorporation of information from underneath the clouds, which contain information inherently linked to the rainfall-generating mechanisms. Such information is more strongly correlated with near-surface precipitation intensities than cloud-top characteristics. This is especially challenging over the western contiguous United States (CONUS) where current IR-based precipitation products fail to capture rainfall events accurately. One difficulty such algorithms face, especially over the western CONUS, is the various regimes of rainfall over the region: nonbrightband (NBB) rainfall, brightband (BB) rainfall, and hybrid rainfall (White et al. 2003). Clouds associated with NBB precipitation frequently occur at lower levels than BB rainfall-associated clouds with temperatures of ~250–270 K and have a strong correlation with orographic lifting (Neiman et al. 2005; Martner et al. 2008; Matrosov et al. 2014). For example, Neiman et al. (2005) found that NBB rainfall contributes significantly (18%–50%) to the yearly wintertime precipitation totals in the mountainous study region of Cazadero, California. While the designation between BB and NBB has its roots in radar retrievals rather than from satellite remote sensing, Neiman et al. (2005) shows that NBB rainfall- and BB rainfall-producing clouds' T_b values can differ by tens of kelvins while producing identical rainfall totals. Thus, NBB rainfall must be made a primary consideration in any precipitation-measuring studies in the region. However, as all measurements taken in this study are in regard to temperature and not reflectivity, the authors from henceforth will refer to shallow, higher-temperature, orographically linked precipitation as warm precipitation rather than NBB precipitation.

To illustrate the difficulty of rainfall detection in the region, Nguyen et al. (2018) showed that PERSIANN products generally have good performance over the CONUS except in some areas in Nevada, Oregon, the Central Valley (California), and parts of Northern California. Similarly, Ombadi et al. (2018) highlighted the challenges associated with using PERSIANN

Climate Data Record (CDR) over California for hydrological and engineering applications due to its deficiencies in detecting extreme rainfall. Owing to these errors, the study concluded that there are limitations in developing intensity–duration–frequency (IDF) curves over some regions of the western CONUS.

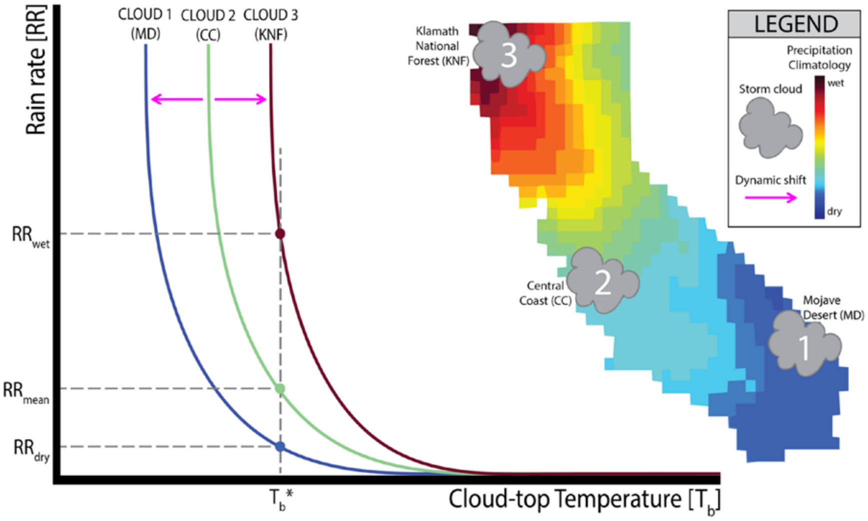

Fig. 1. The dynamic cloud-top brightness temperature (T_b)–rain rate (RR) model. In PERSIANN-CCS, clouds that are identical in shape, size, temperature distribution, and all other defining characteristics but spatial location have completely identical RR readings. However, in PDIR, the underlying climatology causes shifts in the T_b–RR curves that characterize cloud-based models like PERSIANN-CCS and PDIR. In PDIR, drier climatologies such as the Mojave Desert (MD) cause a leftward shift in the T_b–RR relationships, which results in lower precipitation rates than at identical temperatures in moderately wet regions such as California's Central Coast (CC), while wetter climatologies such as the Klamath National Forest (KNF) cause a rightward shift, which causes an increase in estimated precipitation rates for identical temperatures.

In this study, we propose an algorithm that uses rainfall climatology, which is inherently related to local information about the rainfall-generating mechanism, alongside IR-measured T_b to create a model of T_b–RR curves that are dynamically shifted at each pixel according to the relative wetness of the pixel's climatology (Fig. 1). The proposed framework was created through broad modifications and additions to the PERSIANN-CCS algorithm and motivated by the need for accurate detection of heavy precipitation events, especially over the western CONUS. Beyond the dynamic T_b–RR relationship technique, the PERSIANN Dynamic Infrared–Rain rate model (PDIR) further improves upon the PERSIANN-CCS framework by increasing the capture of warm precipitation and cloud patches, adopting monthly cloud-type catalogs, training the dynamic T_b–RR curves with PMW data, and utilizing the shuffled complex evolution optimization algorithm (SCE-UA; Duan et al. 1994) to optimize the dynamic curve model that is PDIR's namesake.

The paper is organized as follows: The second section describes the datasets and domain used in the study; the third section describes the development, training and workflow of PDIR; the fourth section presents evaluation results; and the fifth section highlights the objective, skill, and future directions of PDIR.

Data

In this study, we utilize several datasets for the input, calibration, benchmarking, and comparison of PDIR. PDIR solely utilizes longwave (10.7 μm) from GEOs as input data. For the calibration of the T_b–RR relationships, PDIR utilizes the Combined Microwave precipitation dataset (MWCOMB) obtained from the Climate Prediction Center (CPC), National Oceanic and Atmospheric Administration (NOAA), while rainfall climatology data used for dynamic curve shifting in PDIR's framework come from the WorldClim, version 2, product over land (Fick and Hijmans 2017) and PERSIANN-CDR over water. The dynamic curve fitting is a unique feature in PDIR, which adjusts the precalibrated T_b–RR relationships based on local precipitation climatology. For benchmarking, this study utilized the National Centers for Environmental Prediction (NCEP) Stage IV radar-gauge product. CMORPH (V1.0), TRMM (TMPA 3B42RT), PERSIANN-CCS, and the NCEP Stage II radar-gauge product were selected as comparison

Table 1. Brief descriptions of the precipitation datasets used in this study.

Dataset	Archive period	Spatial resolution (°)	Native temporal resolution	Region
CMORPH V1.0 (Joyce et al. 2004)	1 Jan 1998–present	0.0727	30 min	Quasi global (60°N–60°S)
Stage II/IV (Lin and Mitchell 2005)	1 Jan 2002–present	0.04	1 h	CONUS
MWCOMB (Joyce et al. 2004)	1 Jan 2008–present	0.01	30 min	Quasi global (60°N–60°S)
IMERG V06 "NRT/Early Run" (Huffman et al. 2014)	12 Mar 2014–present	0.1	30 min	Global
PERSIANN-CCS (Hong et al. 2004)	1 Jan 2003–present	0.04	1 h	Quasi global (60°N–60°S)
PERSIANN-CDR (Ashouri et al. 2015)	1 Jan 1983–present	0.25	1 day	Quasi global (60°N–60°S)
TMPA 3B42RT (Huffman et al. 2007)	29 Feb 2000–present	0.25	3-h	Quasi global (60°N–60°S)
WorldClim 2 (Fick and Hijmans 2017)	Climatology	0.01	Monthly	Global

datasets for PDIR. Moreover, IMERG (V06) was used as an additional comparison dataset for the 2018 high-precipitation atmospheric river (AR) event evaluation.

Regarding the benchmarking and comparison datasets, Stage II and Stage IV are primarily radar-based products (though they both have significant gauge components; Lin and Mitchell 2005), CMORPH and TRMM utilize PMW and IR as input data, and PERSIANN-CCS solely utilizes IR. IMERG is derived from a combination of multiple satellite precipitation estimating algorithms, which use both IR and PMW data for input. For a more comprehensive summary of the products used in this study, refer to the summary and citations provided in Table 1.

Methodology

Algorithm structure. PDIR is based on the framework of the PERSIANN-CCS system, which is in turn based on the original PERSIANN framework. PERSIANN (Hsu et al. 1997) and PERSIANN-CCS (Hong et al. 2004), along with PERSIANN-CDR (Ashouri et al. 2015), are satellite-based data-driven precipitation estimating systems that work primarily by establishing a link between GEO-derived T_b and RR using machine-learning techniques. The precipitation data products based on these algorithms are available through the Center for Hydrometeorology and Remote Sensing (CHRS) Data Portal (Nguyen et al. 2019). PERSIANN-CCS was created for the purpose of developing a high-spatiotemporal-resolution, near-real-time precipitation dataset that solely utilizes IR data as input.

PERSIANN-CCS diverges from the PERSIANN algorithm by utilizing image segmentation and objective classification methods to process cloud images into cloud-patch regions. Subsequently, the characteristics of segmented cloud-patch regions are extracted and clustered using a self-organizing feature map (SOFM) to create 400 different cloud types, each with characteristic rainfall curves. Both algorithms are discussed in depth in Hsu et al. (1997), Sorooshian et al. (2000), and Hong et al. (2004).

PDIR advances the framework of the PERSIANN-CCS system by (i) improving the capture of warm precipitation by adapting higher temperature thresholds; (ii) introducing gradient filtering and applying morphological filters to improve the watershed method used for segmentation; (iii) expanding the cloud classification system to include monthly sets of cloud types, thus improving the algorithm's ability to distinguish between different rainfall regimes; (iv) improving the skill of the T_b–RR curves with NOAA's PMW dataset; and (v) utilizing gridded climatology data from WorldClim, version 2, and PERSIANN-CDR to create a dynamical T_b–RR curve model, optimized by SCE-UA.

CLOUD PATCHES. Of the issues plaguing the field of remotely sensed precipitation estimation, warm precipitation is one of the most prominent, owing to the low level of contrast between warm cloud temperatures from similar Earth-surface temperatures, along with the lack of ice scattering needed for estimation from PMW. However, as PDIR solely uses IR as input, ice scattering from PMW is not a concern for the algorithm. Therefore, PDIR's sole focus on capturing warm precipitation is to increase the contrast between warm clouds and Earth's surface. As the orography of the western CONUS makes warm rainfall a significant source of yearly precipitation totals in the region, its capture is of high concern.

To capture warm precipitation, PDIR raises the maximum T_b threshold for segmenting from 253 K that is used in PERSIANN-CCS to 273 K. To address the challenge of distinguishing warm precipitating clouds from clear-air pixels with similar brightness temperatures, PDIR has adopted a series of gradient filters and morphology operators designed to increase the contrast around the edges of clouds (Wang 1997; Hayatbini et al. 2019), which improves the effectiveness of the watershed method used to segment cloud patches. This method also increases the effectiveness of cloud segmentation for low-temperature clouds over the original watershed model used in PERSIANN-CCS. While increasing the temperature threshold to 273 K does increase count of false alarms, Karbalaee et al. (2015) found that the increased threshold temperature increases overall skill. Furthermore, this technique has been observed to capture overlapping clouds, for example, a smaller cloud at a higher altitude whose boundary is completely encompassed by a large cloud at a lower altitude, which would normally be captured as one cloud patch in the PERSIANN-CCS system.

CLOUD CLASSIFICATION. The primary innovation that makes PERSIANN-CCS distinct from its parent algorithm is its system of cloud types with characteristic T_b–RR curves. The original PERSIANN-CCS extracts 23 (later reduced to 12) characteristics based on each cloud patch's coldness, geometry, and texture at three different temperature readings (220, 235, and 253 K). These characteristics are fed into the SOFM clustering algorithm to produce 400 distinct cloud types, each with a characteristic nonlinear relationship that relates T_b to RR. More details on the construction of RR curves from the SOFM algorithm can be found in Hong et al. (2004).

In PDIR, to add onto the existing 12 characteristics used in PERSIANN-CCS, IR data greater than 273 K is segmented into cloud patches and the areal extent, average temperature, and three texture characteristics (STD, MSTD^5, and $\mathrm{STD}^5_{\mathrm{std}}$; refer to Hong et al. 2004) are calculated for each cloud patch at the greater temperature threshold, for a total of 17 characteristics. With the addition of warm cloud characteristics, information unique to warm precipitating clouds can be captured and used to distinguish from warm nonprecipitating clouds.

PDIR operates under the assumption that discernable sets of cloud types appear at different stages of the year. Therefore, the algorithm includes twelve trained SOFMs, one for each month, with 100 unique cloud types each, for a total of 1,200 different cloud types. To train each month's set of cloud types, all IR data from one month of each year in the training period (e.g., February of every year) was extracted, along with the second half of the preceding month (e.g., 16–31 January of every year) and the first half of the following month (e.g., 1–15 March of every year). The latter two temporal spans are extracted under the assumption that discernable sets of cloud types can exist later or earlier between years as a result of natural climate variability, and therefore a buffering time is necessary to ensure better training of the monthly cloud-type sets.

T_b–RR RELATIONSHIPS. The central hypothesis behind the creation of PDIR is that characteristics related to the land surface below the clouds (topography, elevation, climate type, temperature climatology, etc.) play a role in the cloud-top temperature–rain rate (T_b–RR) relationship of clouds. Rainfall climatology is used to represent these characteristics as rainfall climatology values are influenced by the unique land surface characteristics inherent to a region. Using this term to "slide" the T_b–RR curve along the T_b axis, we create a dynamic relationship between input IR-measured T_b and output RR. This results in identical clouds with identical

T_b intensities and distributions having different pixel RR values when occupying spaces with differing rainfall climatology (Fig. 1).

Specifically, T_b–RR relationships are created and calibrated following the same procedure as in Hong et al. (2004): five parameters [u^j_{1-5} , Eq. (1)] are trained for each cloud type (j) produced by the SOFM. However, PDIR's RR equation differs from PERSIANN-CCS's with the inclusion of the pixel (i)- and cloud-type-dependent curve-shifting term (Δ) and the increase of cloud types from 400 to 12 sets of 100, for a total of 1,200. Values of RR are constrained to [0, 50], which are the limits of the calibration dataset (Fig. 2):

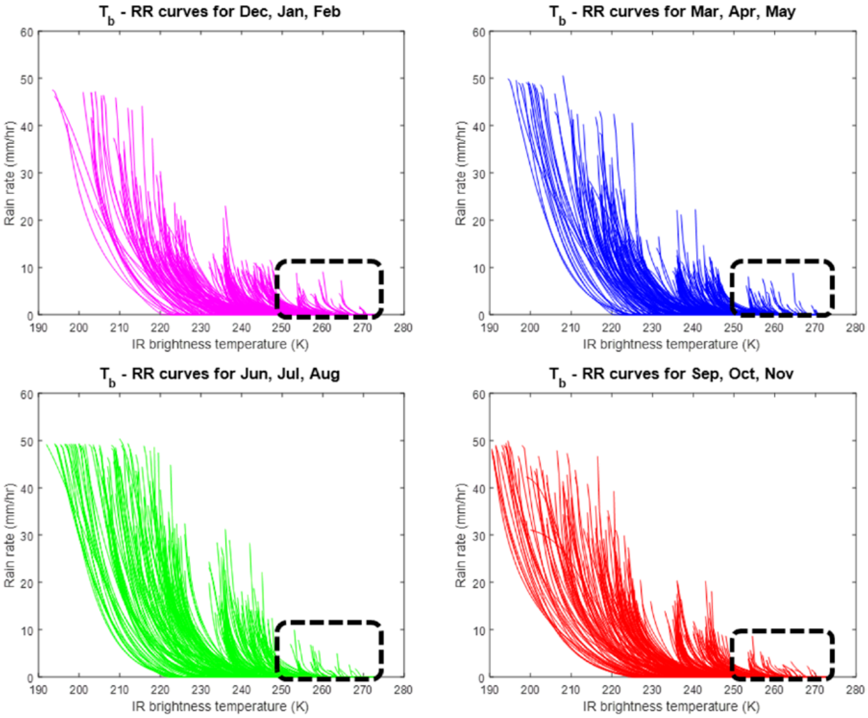

Fig. 2. Seasonal plots of 300 T_b–RR curves produced by the monthly SOFMs. Note the presence of distinct clusters of rainfall curves and the capture of warm precipitation (black dashed boxes) in each season.

$$\mathrm{RR}_i^j = \upsilon_1^j + \upsilon_2^j \exp\left[\upsilon_3^j \max\left(T_i - \Delta_i^j + \upsilon_4^j, 0\right)^{\upsilon_5^j}\right], \qquad (1)$$

where T_b is represented by T_i; Δ is produced from the climatology coefficient γ, a term calculated from dividing rainfall climatology Γ by the mean rainfall climatology of all pixels measured within a cloud type m during calibration. For example, if in the span of 2008–13 there are 2,000 clouds designated cloud-type j extracted from the calibration dataset, then m^j is the sum of the number of pixels in all 2,000 clouds, the cloud-type mean climatology is the average value of rainfall of all pixels in m^j, and the climatology coefficient at any pixel is the climatology at the pixel divided by the mean climatology of the cloud type it is in. Here, Δ is also dependent on two parameter vectors $\boldsymbol{\delta}_1$, $\boldsymbol{\delta}_2$, the target of optimization discussed in the next paragraph:

$$\Delta_i^j = \begin{cases} \delta_1^j\left(1 - \dfrac{1}{\gamma_i^j}\right), & \gamma_i^j \le 1 \\ \delta_2^j\left(\gamma_i^j - 1\right), & \gamma_i^j > 1 \end{cases}, \qquad (2)$$

$$\Upsilon_i^j = \Gamma_i^j \times \left(\sum_{i=1}^{m^j} \frac{\Gamma_i^j}{m^j}\right)^{-1}, \qquad (3)$$

$$\left\{\boldsymbol{\delta}_1 = \left[\delta_1^1, \delta_1^2, \ldots, \delta_1^{1,200}\right], \boldsymbol{\delta}_2 = \left[\delta_2^1, \delta_2^2, \ldots, \delta_2^{1,200}\right]\right\}$$

Optimization of the cloud-shifting technique was performed using the SCE-UA technique. SCE-UA was utilized to find the minimum value of the objective function that is the sum of two parameters a and b, both parameters dependent on $\boldsymbol{\delta}_1$ and $\boldsymbol{\delta}_2$. These parameters modulate the shifting direction and magnitude of the RR curve:

$$\underset{\delta_1,\delta_2}{\arg\min}\, a+b, \text{subject to}: 0 \leq \boldsymbol{\delta}_1 \leq 7.5, 0 \leq \boldsymbol{\delta}_2 \leq 15, \quad (4)$$

where a is the sum of absolute residuals normalized by the sum of all pixel rain rates from the calibration dataset C) (mm) and PDIR rain rates over the same grid (RR). The summation is performed from the linear index of the first pixel to the linear index of the last pixel in the calibration dataset n:

$$a = \frac{\sum_{i=1}^{n} \left| \mathrm{RR}_i - C_i \right|}{\sum_{i=1}^{n} \mathrm{RR}_i + \sum_{i=1}^{n} C_i}; \quad (5)$$

b is the sum of false alarms and misses normalized by the count of all pixels where rainfall was detected by PDIR or where rainfall was not detected by the calibration dataset. Brackets used in the formalization of parameter b are Iverson brackets, which indicate that the value inside the bracket equals 1 when the condition is true and 0 when it is false; "$\wedge$" and "$\vee$" are logical operators for "and" and "or," respectively:

$$b = \frac{\sum_{i=1}^{n} \left[\mathrm{RR}_i > 0.01 \wedge C_i < 0.01 \right] + \sum_{i=1}^{n} \left[\mathrm{RR}_i < 0.01 \wedge C_i > 0.01 \right]}{\sum_{i=1}^{n} \left[\mathrm{RR}_i > 0.01 \vee C_i > 0.01 \right]}. \quad (6)$$

The metrics a and b were chosen through trial and error because they work synergistically to be effective in the calibration of both dry and wet pixels. Optimizing a, a term that effectively captures large errors mostly associated with extreme precipitation, was found to assist PDIR in making more skillful estimates in rainy regions. On the other hand, the term b measures the quantity of pixels where rainfall was incorrectly estimated, a term that is heightened over arid regions where cold clouds frequently do not produce rainfall. As such, optimizing b increases the skill of low-intensity rainfall estimation over dry regions. The range of values that $\boldsymbol{\delta}_1$ can inhabit is smaller than $\boldsymbol{\delta}_2$ because the former term is associated with over-average rainfall climatology and must be more tightly constrained to avoid large overestimations of extremes. The limits of $\boldsymbol{\delta}_1$ and $\boldsymbol{\delta}_2$ were selected from extensive trial-and-error testing during calibration.

The inclusion of the dynamic T_b–RR curve was introduced to combat the failure that satellite precipitation algorithms such as PERSIANN-CCS experience in capturing rainfall accurately in the western CONUS, which has proven difficult due to the highly complex topography in the region. Typically, satellite-based precipitation algorithms underestimate rainfall in the mountain ranges of the West, especially over the Sierra Nevada in California and Nevada; the Cascade Range in Washington, Oregon, and Northern California; and the Pacific coast ranges along the western coast of North America. On the other hand, these same algorithms tend to overestimate rainfall in the dry regions of the American Southwest (Nguyen et al. 2018). By utilizing rainfall climatology with a dynamic rainfall curve model, PDIR can combat these shortcomings and estimate identical rainfall for clouds of differing temperatures, an important feature necessary for the detection of warm precipitation.

PDIR workflow. Brightness temperature IR is read as the sole input by the fully trained PDIR algorithm. After cloud patches are extracted with the assistance of the modified watershed technique, a vector of 17 characteristics is pulled from each cloud patch. The vector is fed into the month's SOFM of cloud types, which returns the most likely cloud type given the extracted characteristics. Each cloud type has a characteristic T_b–RR relationship that is dynamically shifted according to pixel climatology and cloud type before PDIR pulls the final RR estimate. A flowchart of the steps PDIR takes from input to output is included in Fig. 3.

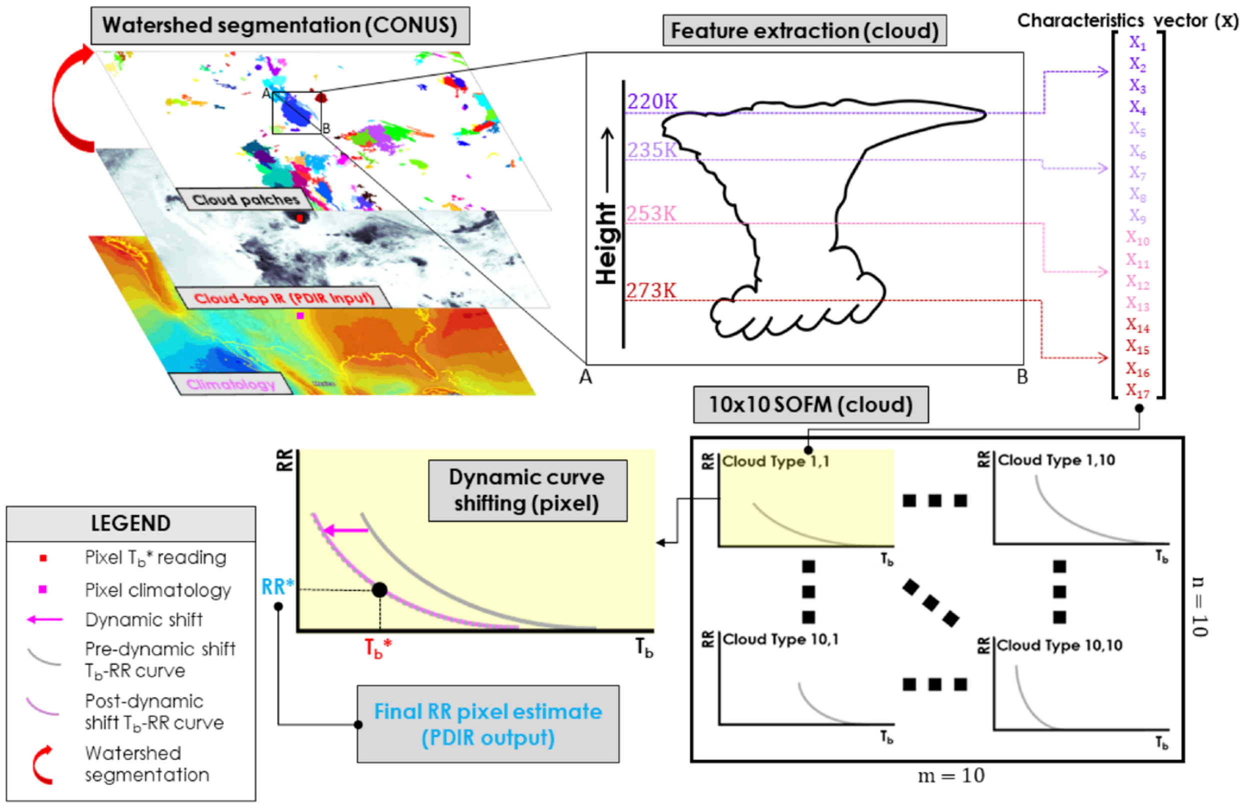

Fig. 3. The workflow of PDIR from input to output.

PDIR's processing starts from large areal scales and gradually decreases down to the pixel level. Input for PDIR is mosaic IR data; after the watershed segmentation step, PDIR begins to work at a cloud-patch level. When the cloud patches are segmented, their characteristics extracted into vectors, and the vector plugged into their respective SOFMs, then PDIR begins to work at the pixel scale, dynamically shifting rainfall curves and extracting RR values. The spatial scales at which different steps of the algorithm are performed are noted in Fig. 3, where "CONUS" signifies the areal extent of the input data used by PDIR (global IR data used by PDIR are clipped to CONUS for the study), "cloud" signifies processing at the cloud-patch level, and "pixel" designates pixel-scale processes.

Calibration and evaluation periods. PDIR's T_b–RR relationships were calibrated during the 2014–16 period and validated for the 2008–13 period by utilizing NOAA's PMW dataset as calibration data. Regarding short-time-scale evaluations, PDIR was additionally evaluated over 20–25 March 2018, the time frame of a large AR event over the west coast of CONUS, for evaluation of its performance during extreme events. PDIR was evaluated against Stage IV and compared with Stage II, PERSIANN-CCS, CMORPH, and TRMM from 2008 to 2013. PDIR and other precipitation datasets used for evaluation and comparison in this study have different spatial and temporal resolutions. To account for these differences, all products were rescaled to 0.25° × 0.25° with a daily temporal resolution. However, for evaluation of PDIR in capturing AR events, all products were rescaled to 0.04° × 0.04° and 6-hourly spatial and temporal resolutions, respectively. All rescaling (upscaling or downscaling) was performed using bilinear interpolation.

Results and discussion

PDIR estimates were validated over the western CONUS at the annual and daily level during the validation period of 2008–13. In addition, short-time-scale validation was performed for two specific extreme AR events, as ARs are intimately related to water resources and natural hazards in Pacific coast states (Dettinger 2013).

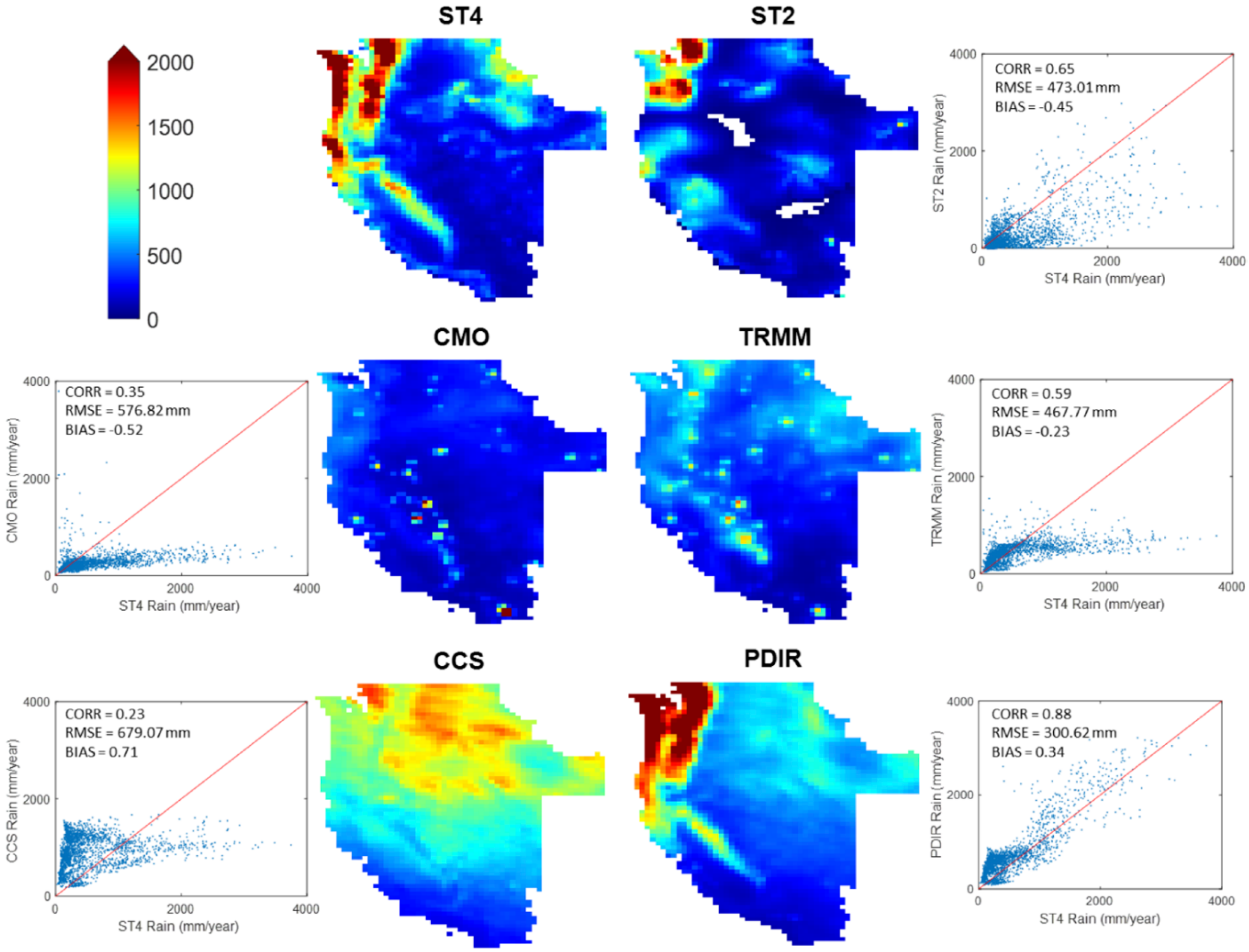

Fig. 4. Average annual rainfall (mm year^{-1}) for the validation period (2008–13) for the baseline product Stage IV (ST4), the near-real-time Stage II (ST2), the three satellite-based precipitation products [CMORPH (CMO), TRMM, and PERSIANN-CCS (CCS)], and the new product, PDIR.

For the validation results that follow, Stage IV was used as a benchmark for validation because the dataset incorporates quality-controlled rainfall information from ground gauges and radars, which provides a high-quality product with a rich spatiotemporal resolution. While Stage IV is the main baseline for validation, Stage II was used as a benchmark when the validation was performed for near-real-time estimates (i.e., daily), which are important to disaster decision-making strategies during extreme storm events. The decision to use Stage II as the validation benchmark for AR events, which frequently cause flash flooding, is because Stage II is a real-time dataset. In such a comparison, our intent is to assess the performance of satellite-based products for near-real-time applications. Other products used for comparison purposes include PERSIANN-CCS, CMORPH, TRMM, and IMERG (for one AR event).

Validation across several temporal domains. Comparisons of the average annual accumulated rainfall totals during the validation period over the western CONUS (i.e., the states of California, Oregon, Washington, Nevada, and Idaho) are presented in Fig. 4. The results indicate that the three satellite-based precipitation products (CMORPH, TRMM, and PERSIANN-CCS) fail to reproduce the patterns of spatial variability in precipitation that are observed in the baseline product Stage IV. As observable from the maps and scatterplots in Fig. 4, CMORPH, TRMM, and PERSIANN-CCS all severely underestimate rainfall over the rainy northwestern regions of the Pacific coast states (the Cascade Range and Sierra Nevada). Moreover, PERSIANN-CCS overestimates rainfall over Idaho and the eastern parts of Washington and Oregon. On the other hand, PDIR accurately reproduces spatial patterns of rainfall that are similar to the observed ones, with high rainfall totals over the Cascade Range and Sierra Nevada as well as moderate rainfall over northwestern Idaho. Apart from slight overestimation over arid parts of Nevada, PDIR provides accurate rainfall spatial variability at the annual scale with a correlation coefficient (CORR) of 0.88 compared to 0.35, 0.23, 0.65, and 0.59 for CMORPH, PERSIANN-CCS, Stage II, and TRMM, respectively. It is worth noting that PDIR also has superior performance compared to the near-real-time, multisensor (i.e., radar and gauges) Stage II. Overall, these evaluation results highlight the difficulty of observing rainfall from satellites over the complex and heterogeneous topography of the western CONUS, as evidenced by most satellite-based precipitation products' tendency to either severely underestimate or overestimate rainfall even at long temporal accumulation periods (i.e., annual).

Despite the usefulness that validation at the annual scale has in providing an overall view of the performance of the products, shorter temporal scales such as daily, monthly, and seasonal are most relevant for hydrologic applications. Thus, Figs. 5–7 shed light on the performance of PDIR in comparison to other satellite-based precipitation products, as well as Stage II. Figure 5 demonstrates the performance of PDIR in terms of continuous comparison metrics, namely CORR, root-mean-square error (RMSE), and relative bias (BIAS). Unsurprisingly, Stage II has the highest CORR since it is one of the input data used to produce Stage IV. PDIR, on average, has a CORR of (0.41) compared to 0.45, 0.47, and 0.40 for CMORPH, TRMM, and PERSIANN-CCS, respectively (See Table 2). In addition, PDIR, with a BIAS value of 0.89, is significantly better than TRMM (1.88) and PERSIANN-CCS (2.03), but has a greater magnitude than CMORPH (−0.29). As for the RMSE, CMORPH, TRMM, and PDIR, all show approximately similar patterns with higher errors over regions with heavier rainfall. These subtle differences between the products' performances at the daily scale do not corroborate the discrepancies observed at the annual scale (Fig. 4). This led us to investigate to what extent each satellite-based precipitation product's performance is dependent on the quantity of rainfall measured.

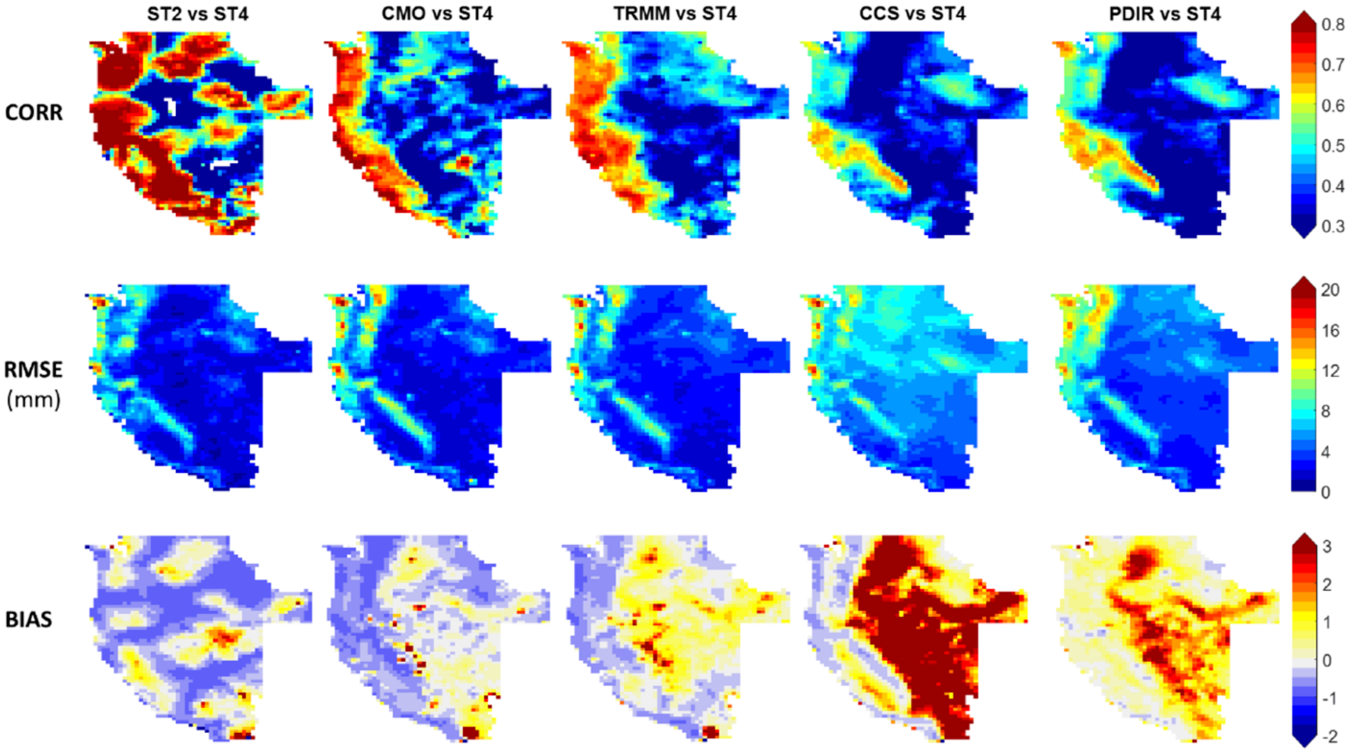

Fig. 5. Continuous comparison metrics for daily rainfall: (top) correlation (CORR), (middle) root-mean-square error (RMSE), and (bottom) multiplicative bias (BIAS) for (left to right) the near-real-time Stage II, the three satellite-based precipitation products [CMORPH (CMO), TRMM, and PERSIANN-CCS (CCS)], and the new product, PDIR.

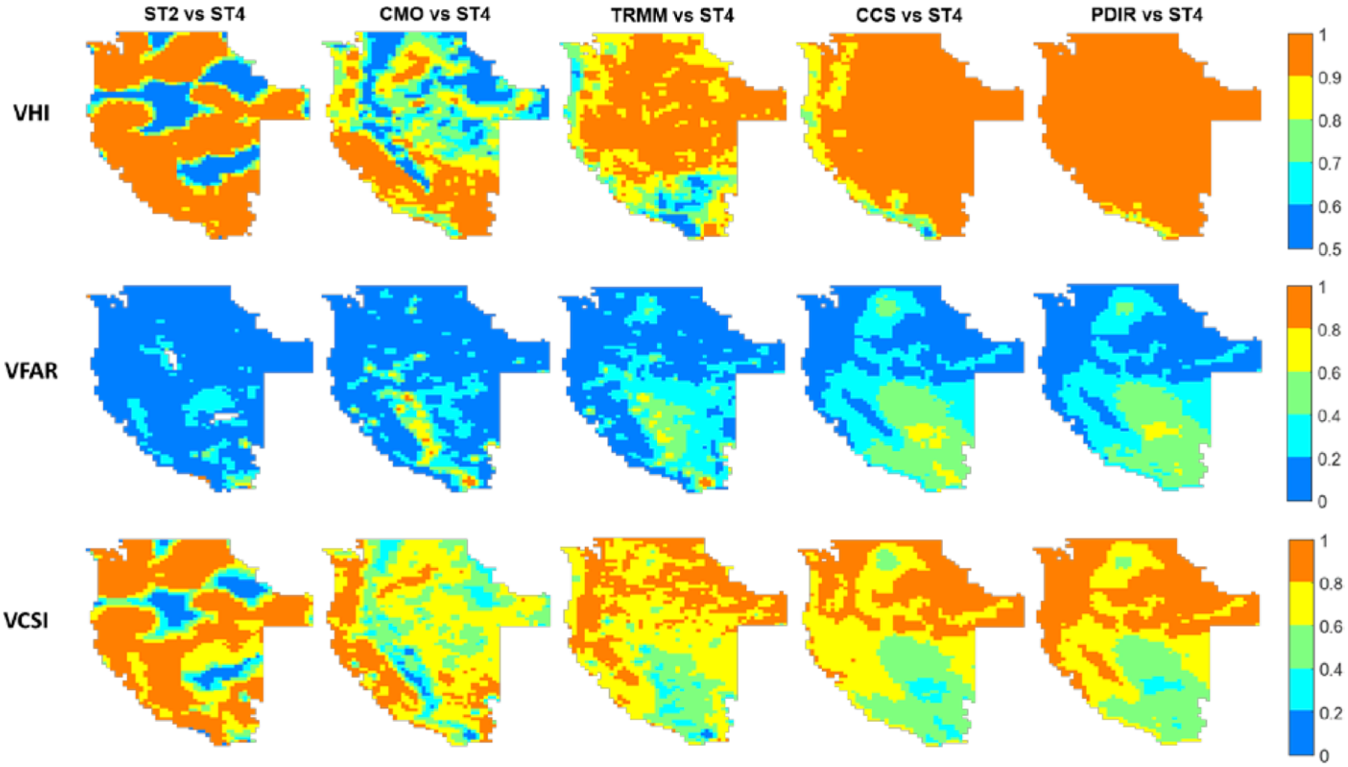

Fig. 6. Volumetric categorical indices for daily rainfall: (top) volumetric iit index (VHI), (middle) volumetric false alarm ratio (VFAR), and (bottom) volumetric critical success index (VCSI) for (left to right) the near-real-time Stage II, the three satellite-based precipitation products [CMORPH (CMO), TRMM, and PERSIANN-CCS (CCS)] and the new product, PDIR.

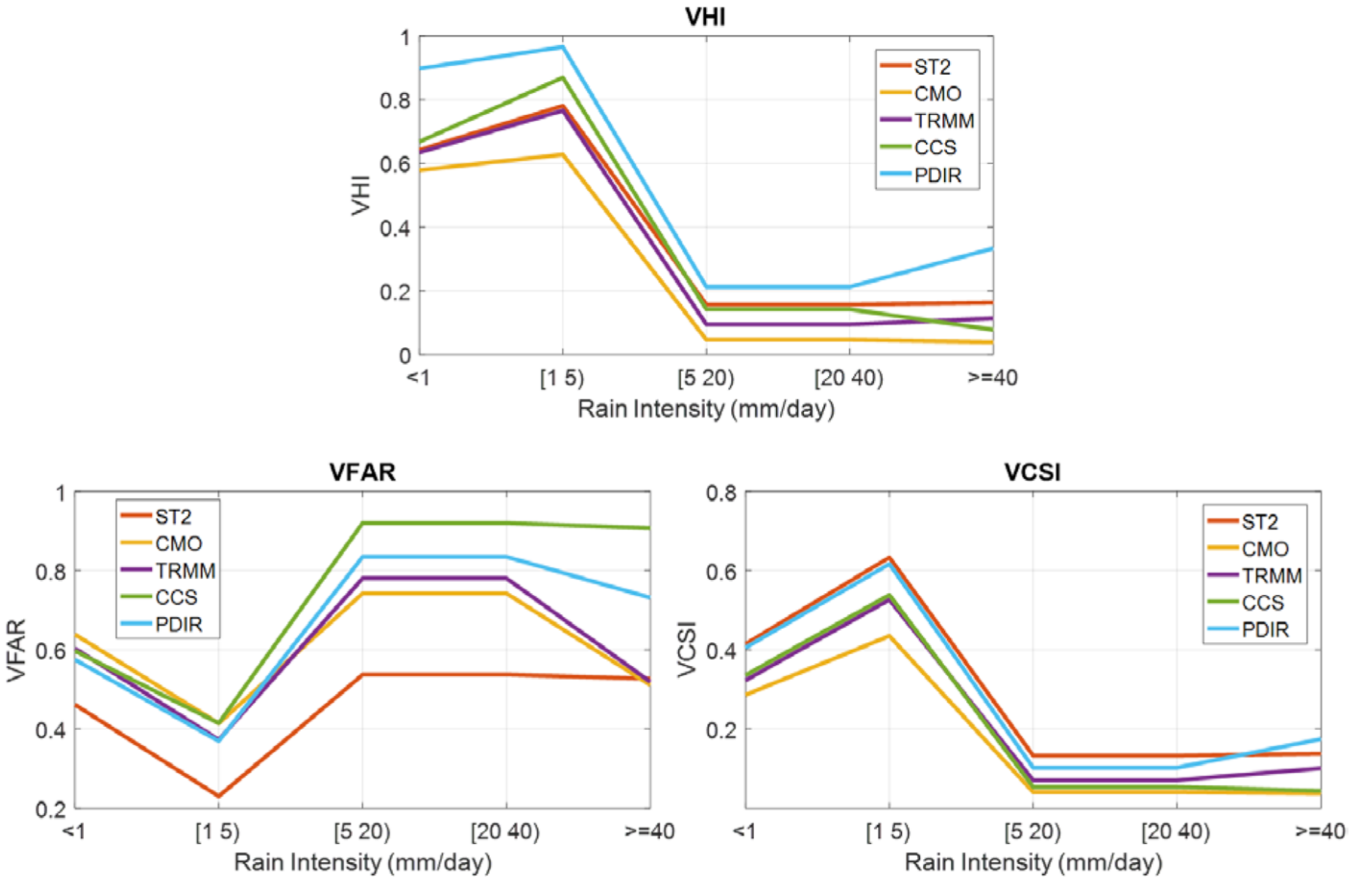

Fig. 7. Volumetric categorical comparison statistics of daily rainfall (2008–13) with different rainfall intensities.

Table 2. Summary statistics of comparison metrics: (top row) mean daily precipitation (precip); (next three, shaded rows) spatially averaged continuous correlation (CORR), root-mean-square error (RMSE), and multiplicative bias (BIAS); and (bottom three rows) spatially averaged categorical volumetric hit index (VHI), volumetric false alarm ratio (VFAR), and volumetric critical success index (VCSI). The new model (PDIR) is highlighted in boldface in the last column.

Metrics	Stage IV	Stage II	CMORPH	TRMM	CCS	PDIR
Mean daily precip (mm)	1.65	0.83	0.75	1.19	2.53	2.20
CORR	—	0.58	0.45	0.47	0.40	0.41
RMSE (mm)	—	0.36	4.11	4.33	6.40	5.30
BIAS	—	−0.29	−0.24	1.88	2.03	0.89
VHI	—	0.76	0.68	0.72	0.78	0.90
VFAR	—	0.33	0.44	0.40	0.36	0.42
VCSI	—	0.53	0.42	0.47	0.52	0.54

To test this hypothesis, we examine the performance of each product in detecting heavy and light rainfall separately utilizing volumetric categorical indices, namely, volumetric hit index (VHI), volumetric false alarm ratio (VFAR), and volumetric critical success index (VCSI). These indices were proposed by AghaKouchak and Mehran (2013) and are intended to diagnose the products' performances based on the volume of captured rain as opposed to the occurrence of rainfall that is used in conventional categorical metrics [e.g., probability of detection (POD), FAR, critical success index (CSI)]. PDIR shows a significantly higher value of VHI (0.90) compared to the values of 0.68, 0.72, and 0.78 for CMORPH, TRMM, and PERSIANN-CCS, respectively. A VHI value of 1.00 indicates that the volume of observed rainfall is correctly detected compared to the reference dataset. It is important to interpret VHI in combination with VFAR values since a combination of higher VHI and VFAR values means that the algorithm does not provide improvement in detection skill. VFAR values in Fig. 6 demonstrate that while PDIR significantly improves the volumetric detection of rainfall (VHI), it maintains similar VFAR values to the original PERSIANN-CCS estimates. This indicates that much of the improvement in VHI is the result of enhancing the algorithm skill of detection. The lower values of VHI for CMORPH, TRMM, and PERSIANN-CCS highlight that while these products maintain a high correlation compared to the reference product at the daily scale, they more regularly fail to accurately detect heavy rainfall events over the western CONUS. As VFAR for all satellite products is between the narrow range of 0.36 (PERSIANN-CCS) to 0.44 (CMORPH), the overall performance summarized by VCSI indicates the slight superiority of PDIR. As can be seen in Table 2, PDIR has a higher VCSI with a value of 0.54 compared to 0.42, 0.47, and 0.52 for CMORPH, TRMM, and PERSIANN-CCS, respectively. Indeed, by examining the scatterplots in Fig. 4, one can see that CMORPH, TRMM, and PERSIANN-CCS underestimate heavier rainfall as evidenced by the cluster of points located below the 45° perfect correlation line.

To further evaluate the performance of PDIR in detecting different rainfall intensities compared to other products, the volumetric categorical indices were calculated for several intervals of rainfall intensities <1, [1, 5), [5, 20), [20, 40), and ≥40 mm, the results of which are shown in Fig. 7. It is clear that PDIR is superior to all other products in capturing rainfall over all intervals of rainfall intensity in regard to VCSI values as it maintains a VCSI comparable to Stage II and considerably higher than the other satellite-based products. The values of VHI in Fig. 7 demonstrate that all products including PDIR have lower skill in capturing heavy rainfall (VHI = 0.05–0.4) compared to low rainfall (VHI = 0.6–0.9). Specifically, PDIR significantly improves both the detection of heavy rainfall with VHI of approximately 0.35 for rainfall greater than 40 mm day^{-1} and the detection of low rainfall with VHI of approximately 0.9 for rainfall less than 1 mm day^{-1} and between 1 and 5 mm day^{-1}. It should be noted that while the improvement of PDIR in detecting high rainfall is partly counterbalanced by an increase in false alarms (i.e., VFAR), PDIR is specifically skillful in capturing low rainfall (less than 5 mm) as it returns a greater VHI and a lower VFAR than other products.

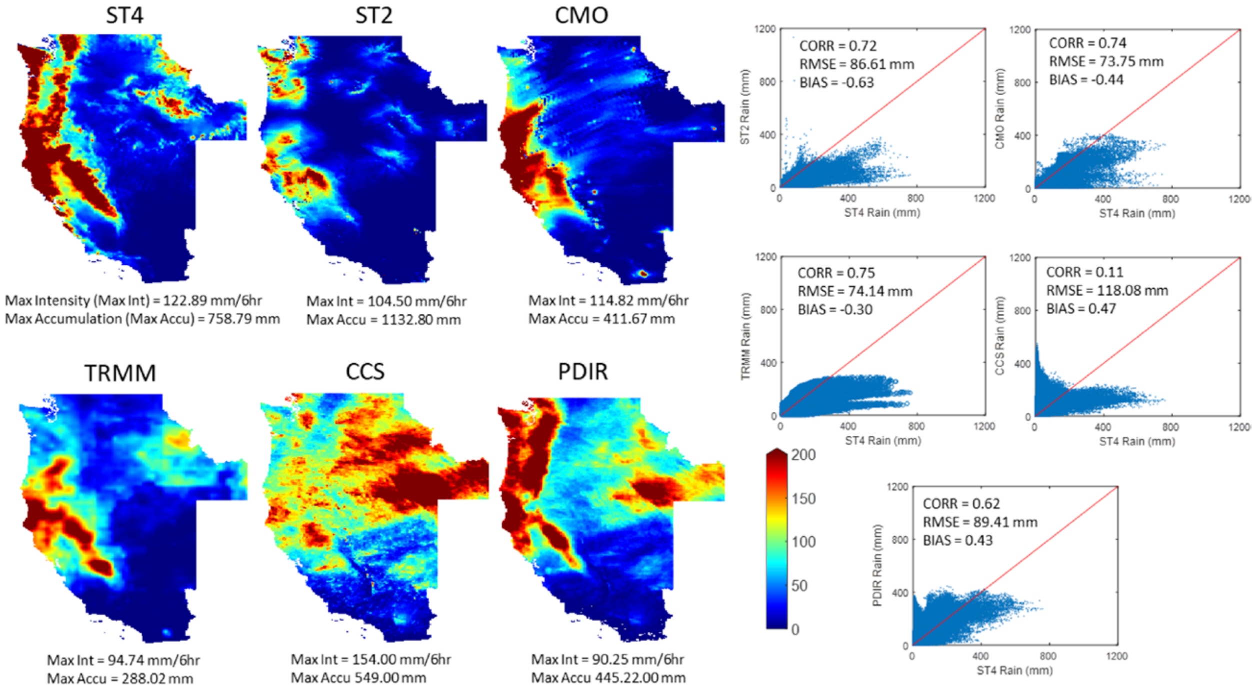

Fig. 8. Rainfall during the period from 28 Nov to 7 Dec 2012 associated with an extreme AR event over California. Six-hourly observations from ground measurements: Stage IV and the near-real-time Stage II, satellite-based measurements: CMORPH (CMO), TRMM, PERSIANN-CCS (CCS), and PDIR.

Extreme atmospheric river events. ARs are transient high-flux corridors of atmospheric water vapor that are a dominant precipitation source for several regions around the globe (Ralph et al. 2006). They are of great significance to the climate, hydrology, and water resources management in the western CONUS owing to their contribution of one-third to one-half of the annual precipitation over much of the region (Dettinger 2013) and their status as the primary source of flooding on the west coast of the CONUS. Ralph et al. (2006) investigated the connection between ARs and flooding in the Russian River basin in California and found that all major floods during the period 1997–2006 were associated with prevalent AR conditions. Thus, accurate observation of precipitation events associated with ARs is of utmost importance for understanding the phenomenon and developing early warning systems for flooding. In this section, we examine the performance of PDIR in detecting the extreme rainfall from two major landfalling ARs.

Atmospheric river event over western CONUS, 28 November–7 December 2012. The AR event from the 2012 North American winter brought with it a series of torrential rainstorms that produced 200 mm of rainfall in 10 days along the coasts of Washington, Oregon, and Northern California. As can be seen in Fig. 8, CMORPH, TRMM, and PERSIANN-CCS inaccurately estimate the spatial patterns and rain totals associated with this storm. Specifically, PERSIANN-CCS's spatial distribution is visually distinct from the evaluation dataset, Stage IV, while the spatial patterns measured by CMORPH and TRMM are more comparable to Stage IV but still see underestimation along the Washington coast. In contrast, PDIR accurately estimates rainfall with a great resemblance to Stage IV spatial rainfall patterns. PDIR slightly underestimates the maximum rainfall intensity with a value of 90.25 mm (6 h)$^{-1}$ compared to the Stage IV's maximum intensity of 123 mm (6 h)$^{-1}$. Although the statistics of CORR, RMSE, and BIAS show that ST2, CMORPH, and TRMM are slightly superior to PDIR in detecting this AR event, the specific advantage of PDIR for this storm is its relatively accurate detection of the storm's spatial variability, aside from some overestimation over southwestern Idaho (likely caused by nonprecipitating cold clouds). Since Stage II is a near-real-time, multisensor

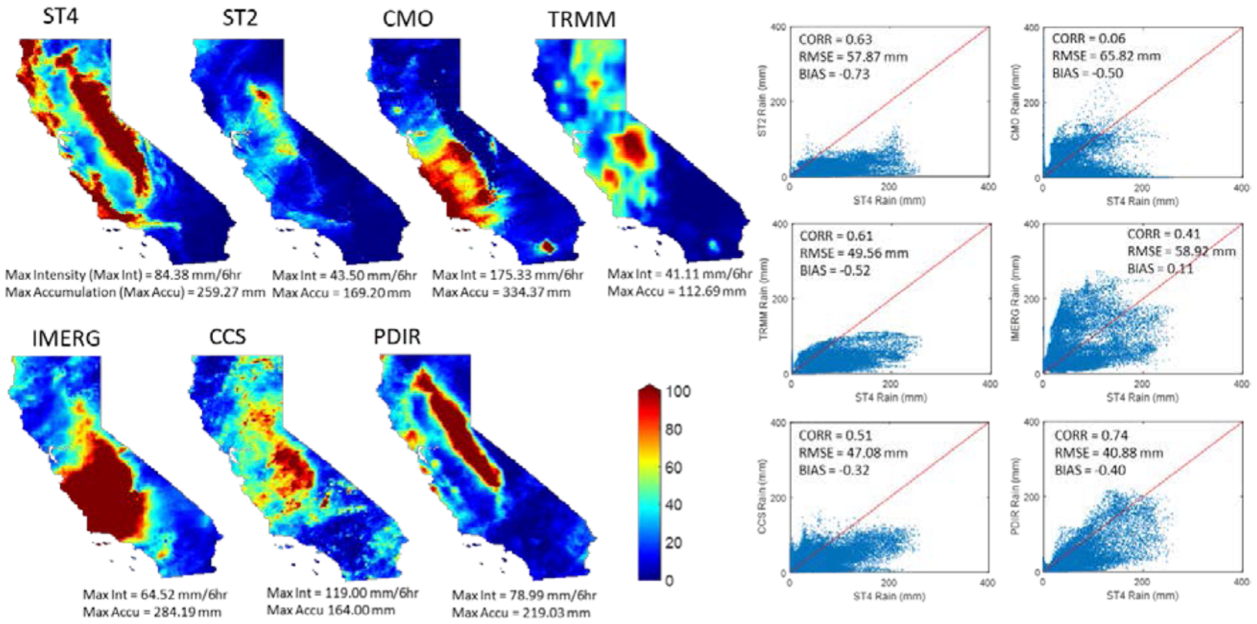

Fig. 9. Rainfall during the period from 20 to 25 Mar 2018 associated with an extreme AR event over California. Observations from ground measurements: Stage IV and the near-real-time Stage II, satellite-based measurements: CMORPH (CMO), TRMM, IMERG, PERSIANN-CCS (CCS), and PDIR.

product typically used for natural hazard monitoring, these results suggest that the near-real-time PDIR can be utilized for early warning systems of floods associated with such extreme events as well.

Atmospheric river event over California, 20–25 March 2018. The AR event of 20–25 March 2018 belonged to a specific category of ARs known as the Pineapple Express—these ARs originate over Hawaii, moving from the equatorial Pacific toward the U.S. West Coast. During this period, rainfall totals of 230 mm were recorded in some regions during the first day alone. Figure 9 shows the rainfall accumulation during the 6-day period of the storm. The observed (Stage IV) rainfall spatial pattern consists of a band of heavy rainfall along the Sierra Nevada and disconnected bands of heavy rainfall along the California coast. Although all satellite-based products (CMORPH, TRMM, IMERG, and PERSIANN-CCS) estimate heavy rainfall during the storm period, PDIR is the only product to mimic the observed spatial rainfall patterns, apart from underestimation over the northern coast of California. In addition to a better spatial pattern, PDIR estimates more accurate rainfall amounts than other products with CORR of 0.74 and RMSE of 41 mm. PDIR is superior to Stage II in detecting the heavy storm rainfall in terms of both spatial patterns and volume. In addition to the metrics just discussed, PDIR has a BIAS of −0.40, which are superior to Stage II's CORR, RMSE, and BIAS values of 0.63, 57.87 mm, and −0.73. This is consistent with the findings in the previous subsection and shows that PDIR has potential benefits in storm monitoring, designing of early warning systems, and disaster management planning for heavy storms associated with ARs over the west coast of the CONUS.

Conclusions and future direction

In this study, we introduced a remotely sensed precipitation algorithm that solely utilizes IR as input data and proved that it was of comparable or greater relative skill to PMW-, radar-, and other IR-based products for annual accumulations and short-term extreme weather events. Furthermore, PDIR accurately mimics the observed spatial patterns of rainfall over the study region, notably the high rainfall amounts over the Cascade Range and Sierra Nevada. PDIR's noteworthy performance in capturing the western CONUS's rainfall, especially with high intensities and over mountainous regions, suggests a level of success in adapting to the challenges of the differing rainfall regimes that are intrinsic to the area. However, analysis into PDIR's skill specific to each rainfall regime must be undergone before concrete conclusions are made.

Of particular interest is that PDIR yields rainfall estimates for extreme rainfall events that are comparable to the nearly instantaneous, multisensor product Stage II with a CORR of 0.62 (first AR event) and 0.74 (second AR event) compared to Stage II's CORR of 0.72 and 0.63. Furthermore, the spatial patterns of PDIR's precipitation estimates in mountainous regions better mimic those recorded by Stage IV than those shown by Stage II. The implications that this algorithm's success at these scales suggests are significant: PDIR contains the spatiotemporal richness and near-instantaneous availability (from 15 min to 1 h) necessary for rapid hazard response while showing potential to have enough skill to be useful for hydrologic and water resources applications, of which the latter has been a major weakness of IR-based algorithms to date.

Despite its strengths, PDIR, like its parent algorithm PERSIANN-CCS, still has the tendency to regularly overestimate rainfall totals (see BIAS in Table 2) and falsely detect rainfall (Fig. 8). Moreover, PDIR's skill on the Pacific coast is eclipsed by other products at the daily scale. When examining these weaknesses, it is important to remember that making comparisons between satellite products that solely utilize IR as input to multisensor products is in a sense an "apples and oranges" comparison. That is to say, incorporating PMW data as input will always result in an improvement in the skill of that product, which makes any comparison against pure IR products biased. But the shortcomings that PMW data forces onto the product—lower spatiotemporal resolution and longer latency time (3–8 h among the comparison datasets)—mean that its universal utilization for QPE is not strategic. PDIR's comparable strength to IR-PMW products and its weaknesses should be considered with this in mind.

As the implications of this study are valuable to a global audience, PDIR's future direction is chiefly focused on its global implementation. Preliminary evaluations of the global implementation of PDIR show much promise in its global utility for the full breadth of hydrologic applications across temporal scales. Globally implemented PDIR has potential for use in natural disaster management and decision-making related to intense storm events such as hurricanes and monsoons that occur in remote regions and/or regions without accurate near-real-time precipitation measuring systems. Furthermore, as the potential temporal span of PDIR is only dependent on the availability of globally measured IR data, which has been reliably retrieved back to approximately 1983 (Ashouri et al. 2015), there is great potential for the creation of a high-resolution climate data record using PDIR.

Acknowledgments. This research was partially supported by the ICIWaRM of the U.S. Army Corps of Engineers, UNESCO's G-WADI program, Cooperative Institute for Climate and Satellites (CICS) program (NOAA Prime Award NA14NES4320003, Subaward 2014-2913-03) for OHD-NWS student fellowship, Army Research Office (Award W911NF-11-1-0422), National Science Foundation (NSF Award 1331915), Department of Energy (DOE Prime Award DE-IA0000018), California Energy Commission (CEC Award 300-15-005), and University of California (4600010378 TO15 Am 22).

References

AghaKouchak, A., and A. Mehran, 2013: Extended contingency table: Performance metrics for satellite observations and climate model simulations. *Water Resour. Res.*, **49**, 7144–7149, https://doi.org/10.1002/wrcr.20498.

Arkin, P. A., and B. N. Meisner, 1987: The relationship between large-scale convective rainfall and cold cloud over the Western Hemisphere during 1982-84. *Mon. Wea. Rev.*, **115**, 51–74, https://doi.org/10.1175/1520-0493(1987)115<0051:TRBLSC>2.0.CO;2.

Ashouri, H., and Coauthors, 2015: PERSIANN-CDR: Daily precipitation climate data record from multisatellite observations for hydrological and climate studies. *Bull. Amer. Meteor. Soc.*, **96**, 69–83, https://doi.org/10.1175/BAMS-D-13-00068.1.

Behrangi, A., B. Khakbaz, T. C. Jaw, A. AghaKouchak, K. Hsu, and S. Sorooshian, 2011: Hydrologic evaluation of satellite precipitation products over a mid-size basin. *J. Hydrol.*, **397**, 225–237, https://doi.org/10.1016/j.jhydrol.2010.11.043.

Dettinger, M. D., 2013: Projections and downscaling of 21st century temperatures, precipitation, radiative fluxes and winds for the southwestern CONUS, with focus on Lake Tahoe. *Climatic Change*, **116**, 17–33, https://doi.org/10.1007/s10584-012-0501-x.

Duan, Q., S. Sorooshian, and V. K. Gupta, 1994: Optimal use of the SCE-UA global optimization method for calibrating watershed models. *J. Hydrol.*, **158**, 265–284, https://doi.org/10.1016/0022-1694(94)90057-4.

Fick, S. E., and R. J. Hijmans, 2017: WorldClim 2: New 1-km spatial resolution climate surfaces for global land areas. *Int. J. Climatol.*, **37**, 4302–4315, https://doi.org/10.1002/joc.5086.

Funk, C., A. Verdin, J. Michaelsen, P. Peterson, D. Pedreros, and G. Husak, 2015: A global satellite assisted precipitation climatology. *Earth Syst. Sci. Data*, **7**, 275–287, https://doi.org/10.5194/essd-7-275-2015.

Hayatbini, N., K.-L. Hsu, S. Sorooshian, Y. Zhang, and F. Zhang, 2019: Effective cloud detection and segmentation using a gradident-based algorithm for satellite imagery: Application to improve PERSIANN-CCS. *J. Hydrometeor.*, **20**, 901–913, https://doi.org/10.1175/JHM-D-18-0197.1.

Hong, Y., K.-L. Hsu, S. Sorooshian, and X. Gao, 2004: Precipitation estimation from remotely sensed imagery using an artificial neural network cloud classification system. *J. Appl. Meteor.*, **43**, 1834–1853, https://doi.org/10.1175/JAM2173.1.

——, R. F. Adler, A. J. Negri, and G. J. Huffman, 2007: Flood and landslide applications of near real-time satellite rainfall products. *Nat. Hazards*, **43**, 285–294, https://doi.org/10.1007/s11069-006-9106-x.

Hsu, K.-L., X. Gao, S. Sorooshian, and V. Gupta, 1997: Precipitation estimation from remotely sensed information using artificial neural networks. *J. Appl. Meteor.*, **36**, 1176–1190, https://doi.org/10.1175/1520-0450(1997)036<1176:PEFRSI>2.0.CO;2.

Huffman, G. J., and Coauthors, 2007: The TRMM Multisatellite Precipitation Analysis (TMPA): Quasi-global, multiyear, combined-sensor precipitation estimates at fine scales. *J. Hydrometeor.*, **8**, 38–55, https://doi.org/10.1175/JHM560.1.

——, D. T. Bolvin, D. Braithwaite, K. Hsu, R. Joyce, C. Kidd, E. J. Nelkin, and P. Xie, 2014: NASA Global Precipitation Measurement (GPM) Integrated Multi-Satellite Retrievals for GPM (IMERG). NASA/GSFC Algorithm Theoretical Basis Doc., 31 pp.

Joyce, R. J., J. E. Janowiak, P. A. Arkin, and P. Xie, 2004: CMORPH: A method that produces global precipitation estimates from passive microwave and infrared data at high spatial and temporal resolution. *J. Hydrometeor.*, **5**, 487–503, https://doi.org/10.1175/1525-7541(2004)005<0487:CAMTPG>2.0.CO;2.

Karbalaee, N., K. Hsu, and S. Sorooshian, 2015: Improving warm rain estimation in the PERSIANN-CCS satellite-based retrieval algorithm. *2015 Fall Meeting*, San Francisco, CA, Amer. Geophys. Union, Abstract H21M-08.

Kuligowski, R. J., 2002: A self-calibrating real-time GOES rainfall algorithm for short-term rainfall estimates. *J. Hydrometeor.*, **3**, 112–130, https://doi.org/10.1175/1525-7541(2002)003<0112:ASCRTG>2.0.CO;2.

Lin, Y., and K. E. Mitchell, 2005: The NCEP Stage II/IV hourly precipitation analyses: Development and applications. *19th Conf. Hydrology*, San Diego, CA, Amer. Meteor. Soc., 1.2, https://ams.confex.com/ams/pdfpapers/83847.pdf.

Martner, B. E., S. E. Yuter, A. B. White, S. Y. Matrosov, D. E. Kingsmill, and F. M. Ralph, 2008: Raindrop size distributions and rain characteristics in California coastal rainfall for periods with and without a radar bright band. *J. Hydrometeor.*, **9**, 408–425, https://doi.org/10.1175/2007JHM924.1.

Matrosov, S. Y., F. M. Ralph, P. J. Neiman, and A. B. White, 2014: Quantitative assessment of operational weather radar rainfall estimates over California's northern Sonoma County using HMT-West data. *J. Hydrometeor.*, **15**, 393–410, https://doi.org/10.1175/JHM-D-13-045.1.

Neiman, P. J., B. E. Martner, A. B. White, G. A. Wick, F. M. Ralph, and D. E. Kingsmill, 2005: Wintertime nonbrightband rain in California and Oregon during CALJET and PACJET: Geographic, interannual, and synoptic variability. *Mon. Wea. Rev.*, **133**, 1199–1223, https://doi.org/10.1175/MWR2919.1.

Nguyen, P., S. Sellars, A. Thorstensen, Y. Tao, H. Ashouri, D. Braithwaite, K. Hsu, and S. Sorooshian, 2014: Satellites track precipitation of super typhoon Haiyan. *Eos, Trans. Amer. Geophys. Union*, **95**, 133–135, https://doi.org/10.1002/2014EO160002.

——, M. Ombadi, S. Sorooshian, K. Hsu, A. AghaKouchak, D. Brathwaite, H. Ashouri, and A. R. Thorstensen, 2018: The PERSIANN family of global satellite precipitation data: A review and evaluation of products. *Hydrol. Earth Syst. Sci.*, **22**, 5801–5816, https://doi.org/10.5194/hess-22-5801-2018.

——, and Coauthors, 2019: The CHRS Data Portal, an easily accessible public repository for PERSIANN global satellite precipitation data. *Sci. Data*, **6**, 180296, https://doi.org/10.1038/sdata.2018.296.

Ombadi, M., P. Nguyen, S. Sorooshian, and K.-L. Hsu, 2018: Developing intensity-duration-frequency (IDF) curves from satellite-based precipitation: Methodology and evaluation. *Water Resour. Res.*, **54**, 7752–7766, https://doi.org/10.1029/2018WR022929.

Ralph, F. M., P. J. Neiman, G. A. Wick, S. I. Gutman, M. D. Dettinger, D. R. Cayan, and A. B. White, 2006: Flooding on California's Russian River: Role of atmospheric rivers. *Geophys. Res. Lett.*, **33**, L13801, https://doi.org/10.1029/2006GL026689.

Scofield, R. A., and R. J. Kuligowski, 2003: Status and outlook of operational satellite precipitation algorithms for extreme-precipitation events. *Wea. Forecasting*, **18**, 1037–1051, https://doi.org/10.1175/1520-0434(2003)018<1037:SAOOS>2.0.CO;2.

Sorooshian, S., K.-L. Hsu, X. Gao, H. V. Gupta, B. Imam, and D. Braithwaite, 2000: Evaluation of PERSIANN system satellite-based estimates of tropical rainfall. *Bull. Amer. Meteor. Soc.*, **81**, 2035–2046, https://doi.org/10.1175/1520-0477(2000)081<2035:EOPSSE>2.3.CO;2.

Sun, Q., C. Miao, Q. Duan, H. Ashouri, S. Sorooshian, and K.-L. Hsu, 2018: A review of global precipitation datasets: Data sources, estimation, and intercomparisons. *Rev. Geophys.*, **56**, 79–107, https://doi.org/10.1002/2017RG000574.

Ushio, T., and Coauthors, 2009: A Kalman filter approach to the Global Satellite Mapping of Precipitation (GSMaP) from combined passive microwave and infrared radiometric data. *J. Meteor. Soc. Japan*, **87A**, 137–151, https://doi.org/10.2151/jmsj.87A.137.

Wang, D., 1997: A multiscale gradient algorithm for image segmentation using watersheds. *Pattern Recognit.*, **30**, 2043–2052, https://doi.org/10.1016/S0031-3203(97)00015-0.

White, A. B., P. J. Neiman, F. M. Ralph, D. E. Kingsmill, and P. O. G. Persson, 2003: Coastal orographic rainfall processes observed by radar during the California Land-Falling Jets Experiment. *J. Hydrometeor.*, **4**, 264–282, https://doi.org/10.1175/1525-7541(2003)4<264:CORPOB>2.0.CO;2.